A novel three-dimensional hydraulic fracturing model based on continuum–discontinuum element method

Xinguang Zhu[a,b], Chun Feng[a,*], Pengda Cheng[a], Xinquan Wang[a,b], Shihai Li[a,b]

[a] *Institute of Mechanics, Chinese Academy of Sciences, Beijing 100190, China*
[b] *University of Chinese Academy of Sciences, School of Engineering Science, Beijing 100049, China*

Abstract

Based on continuum–discontinuum element method (CDEM), a three-dimensional hydraulic fracturing model which can consider simultaneously the continuum field, crack opening, pore seepage field and fracture seepage field is proposed in this paper. In this model, the CDEM method is used to calculate the continuum field and crack opening, and the finite volume method (FVM) is adopted to calculate the seepage field, in which the pore seepage is characterized by Darcy's law and the fracture seepage is expressed by the cubic law. Through the comparison and analysis with four analytical solutions and one experimental phenomenon, the fracture pattern is predicted accurately and the poroelastic stress is captured as well. In addition, the result of a disk with one injection hole suggests that this model can not only depict the fluid pressure distribution in fractures and pores of rock matrix, but also trace the initiation, propagation and intersection of cracks driven by fluid.
© 2021 Elsevier B.V. All rights reserved.

Keywords: Hydraulic fracturing; continuum–discontinuum element method (CDEM); Fracture seepage; Pore seepage; Crack propagation; Numerical simulation

1. Introduction

The research of fracture seepage with leak off is of great significance to the geotechnical engineering. Oil and gas exploitation, landslide prevention, nuclear waste treatment, groundwater pollution prevention and geothermal engineering are all closely related to seepage in geotechnical engineering [1–5].

At present, some progress has been made in the research of fluid–solid coupling seepage problem at home and abroad, which can be divided into theoretical method, experimental method and numerical method according to its research approaches. Since the 1950s, researchers from various countries have put forward different theoretical models, including Terzaghi theory [6], Biot consolidation theory developed based on Terzaghi theory [7,8], the PK model [9], the Perkins–Kern–Nordgren (PKN) model [10], the Khristianovich–Zheltov–Geertsma–De Klerk (KGD) model [11–13], the pseudo-3D (P3D) model [14–16] and the PL3D model [17,18], etc. These models usually assume the crack path in advance and only consider the coupling of solid and fracture seepage without considering the influence of pore seepage and water absorption in rock mass. The approximate solution of the radial hydraulic

---

List of symbols

ϕ	Angle of internal friction (°)
ρ_d, ρ_w	The density of solid, fluid (kg/m^3)
ν	The Poisson's ratio (-)
E	The Young's modulus of solid (Pa)
K	The bulk modulus of fluid (Pa)
k^E, k^F	Permeability coefficient of pore, fracture (m^2 Pa^{-1} s^{-1})
P^E, P^F	Fluid pressure in node of pore, fracture (Pa)
$\overline{P^E}, \overline{P^F}$	Average fluid pressure of pore element, fracture element (Pa)
w	Fracture aperture (m)
κ	The permeability ratio (m^2)
μ	The dynamic viscosity of fluid (Pa s)
s^E, s^F	Fluid saturation of node of pore, fracture (-)
$\overline{s^E}, \overline{s^F}$	Fluid saturation of element of pore, fracture (-)
n	Porosity of rock matrix (-)
Q^E, Q^F	Flow rate of node of pore, fracture (m^3 s^{-1})
N^E, N^F	The total number of nodes per pore element, fracture element (m^3 s^{-1})
K_{Ic}	The model I fracture toughness of the rock (Pa^3 m$^{1/2}$)

---

fracture (penny-shaped) model was obtained by [19–22], whose behavior is determined by a combined interplay of fluid viscosity, fracture toughness, and fluid leak-off. Although it is difficult to simulate complex propagation, it has a great advantage in solving the fluid–solid coupling seepage problems involving water absorption in rock mass. The study of fluid–solid coupling seepage based on experiment is not only costly, but also tedious and time-consuming. As a result, more accurate numerical methods have been used to simulate hydraulic fracturing problems since the 1980s.

The typical examples of fluid–solid coupled seepage numerical method based on continuum mechanics include displacement discontinuity method (DDM) [23,24], finite element method (FEM) [25,26], extended finite element method (XFEM) [27–31] and implicit level set algorithm (ILSA) [32,33] and so on. [34] used DDM to simulate hydraulic fracturing, in which fluid can flow through closed natural fractures, but still without considering the permeability of the rock itself. [35] used FEM to simulate plane-strain, straight hydraulic fractures in an impermeable elastic medium. However, the problem with the finite element method is that the mesh must be in accordance with the boundary of the cracks, which will require constant remeshing to trace the crack propagation. And the mapping of physical information between the old and new meshes after remeshing will lead to the decrease of computational accuracy. [36] proposed a fully coupled three-phase model for hydraulic fracturing of porous media based on XFEM. In this model, XFEM is used to treat discontinuations and a cohesive crack model is used as a fracturing criterion. Although XFEM can avoid re-meshing, it requires a very fine mesh in the solution domain, which consumes a lot of computing time when the crack path is unknown in advance. As a result, it is difficult to simulate complex propagation and intersection of multiple cracks using XFEM.

The representatives of fluid–solid coupled seepage numerical method based on discontinuum mechanics include discrete element method(DEM) [37] and discontinuous deformation analysis (DDA) [38]. The basic idea of DEM is to divide the zone studied into a collection of blocks (particles), which are connected by contact springs. And the contact state of blocks (particles) should be updated in real time in the process of movement, to describe the motion state of the whole system. DDA is a new numerical method following DEM. DDA is somewhat similar to the finite element method for solving stress–displacement problems, but accounts for the interaction of independent blocks (particles) along discontinuities in fractured and jointed rock masses. With strict theory and high precision, this method can not only calculate the small deformation before the failure, but also calculate the large displacement after the failure, which is very effective to solve the problem of rock fracture and movement. By coupling these two methods with the hydraulic model, they can be used to simulate the hydraulic fracturing problem. For example,
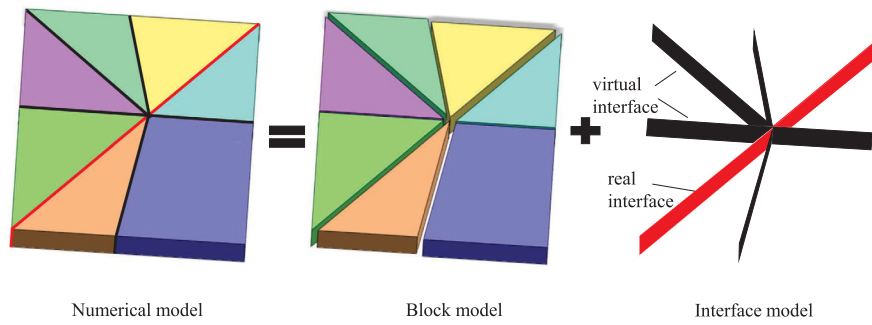
Fig. 1. Schematic diagram of CDEM.

[39] combine DEM with the SRM model to simulate the fracture of complete rock and the opening and sliding process of the initial cracks under hydraulic fracturing. Based on the traditional DDA model, [40] added a fluid network model to realize the simulation of fracture initiation and propagation in hydraulic fracturing. However, it is worth mentioning that the above method only considers the flow of fluid in fractures, but does not consider the seepage process of pore matrix in rock mass.

To overcome the defects of the above methods in simulating hydraulic fracturing, a novel three-dimensional hydraulic fracturing model based on continuum–discontinuum element method (CDEM–HF3D) is proposed in this paper, which not only includes the fracture seepage of fluid flow in joints or fractures, but also the pore seepage in the rock mass and the coupling between them. This model can also simulate the whole process of cracks from initiation, propagation to intersection driven by fluid.

This paper is organized as follows: First, the basic knowledge of CDEM is briefly introduced in Section 2. Section 3 introduces the basic assumptions and concepts of the CDEM–HF3D and the algorithms of pore seepage, fracture seepage, pore–fracture seepage, solid–pore seepage and solid–fracture seepage. In Section 4, six cases are given to verify the correctness and validity of the model proposed in this paper.

2. CDEM profile

CDEM [41,42] is an explicit numerical analysis method coupled with finite element method and discrete element method. It is mainly used in the simulation of progressive failure process of rock and soil materials. The advantage of this method is that it can not only simulate the deformation of solid, but also trace the initiation, propagation and penetration of explicit cracks.

2.1. Basic conception of CDEM

As shown in Fig. 1, two basic models are included in the CDEM, namely block model and interface model. The block model is used to represent the continuous properties of the material and can be composed of one or more finite elements. According to the stiffness matrix of the finite element, the stiffness matrix of any block can be calculated, and there is no need to form an overall stiffness matrix between blocks. Dynamic relaxation technology is adopted to solve the physical information of displacement and stress of each block element. The interface model is used to characterize the discontinuous properties of materials and include real contact surface and virtual contact surface. The interface between blocks is expressed by the real contact surface, which can represent joints and faults in the rock mass, whereas the interface between the internal elements of blocks is expressed by the virtual contact surface, which provides a potential fracture channel for the failure of the continuous part of the rock mass. The blocks on both sides of the contact surface are connected by contact springs, and each contact is connected by a normal spring and two tangential springs (3D). The break of the blocks and elements is realized by the spring fracture between the interfaces, and then the progressive failure process of the model material from continuous to discontinuous.

2.2. The solution of block model

In the calculation of block model, the spatial domain is discretized into blocks, and each block contains one or more finite elements, which are used to represent the continuous properties of materials. For each finite element in the spatial domain, the governing equation can be expressed as

$$\boldsymbol{M}\ddot{\boldsymbol{u}}^e + \boldsymbol{C}\dot{\boldsymbol{u}}^e + \boldsymbol{K}\boldsymbol{u}^e = \boldsymbol{F}^e, \tag{1}$$

where $\boldsymbol{M}$ represents the concentrated mass matrix, $\boldsymbol{C}$ represents the damping matrix, $\boldsymbol{K}$ represents the element stiffness matrix, $\boldsymbol{u}^e$ represents the element displacement vector, and $\boldsymbol{F}^e$ represents the element external force vector, including the solid force and fluid pressure.

In the time domain, Euler's forward difference method is used for explicit iterative solution, and the difference form is

$$\begin{cases} \dot{\boldsymbol{u}}^{n+1} = \dot{\boldsymbol{u}}^{n+1} + \ddot{\boldsymbol{u}}\,\Delta t, \\ \boldsymbol{u}^{n+1} = \boldsymbol{u}^{n+1} + \dot{\boldsymbol{u}}\,\Delta t. \end{cases} \tag{2}$$

2.3. The solution of interface model

Interfaces between finite elements within blocks are used to characterize the discontinuous properties of materials. The relative displacement of the contact point of adjacent elements and the spring force satisfy Hooke's law:

$$\begin{cases} \Delta u_n = \dfrac{F_n}{K_n} = \dfrac{(\sigma_{n1} + \sigma_{n2})A}{2K_n}, \\ \Delta u_\tau = \dfrac{F_\tau}{K_\tau} = \dfrac{(\sigma_{\tau 1} + \sigma_{\tau 2})A}{2K_\tau}, \end{cases} \tag{3}$$

where $\Delta u_n, \Delta u_\tau$ are the normal and tangential relative displacements respectively. F_n, F_τ are the normal and tangential forces respectively. σ_{n1}, σ_{n2} are the normal stress of contact point pair. $\sigma_{\tau 1}, \sigma_{\tau 2}$ are the tangential stress of the contact point pair. K_n, K_τ are the normal and tangential stiffness of the spring respectively. A is the area of the contact point pair.

The maximum tensile stress criterion and Mohr–Coulomb criterion are used as the material failure criterion. When the normal stress of the contact point pair is satisfied

$$\sigma_n \geq \sigma_t, \tag{4}$$

tensile failure occurs to the material, and the normal force of the contact point pair is modified as $F_n = 0$. In the above equation, σ_t represents the tensile strength of contact surface.

When the tangential stress of the contact point pair is satisfied

$$\sigma_\tau \geq c + \sigma_n \tan \phi, \tag{5}$$

the material will undergo shear failure, and the tangential force of the contact point pair will be modified to $F_\tau = F_n \tan \phi$.

3. CDEM–HF3D

3.1. Conceptual framework

In the rock mass, the fluid may go deep into the rock block along the joints or fractures, so we assume that the fluid exists in the joints and micro-pores of rock matrix in the CDEM–HF3D, as shown in Fig. 2. The continuum field and pore seepage field are calculated by sharing the solid elements with micropore. And the fracture seepage field is calculated through the fracture elements, which exist on the adjacent surface between the solid elements. This model contains two types of permeability: pore permeability and fracture permeability.
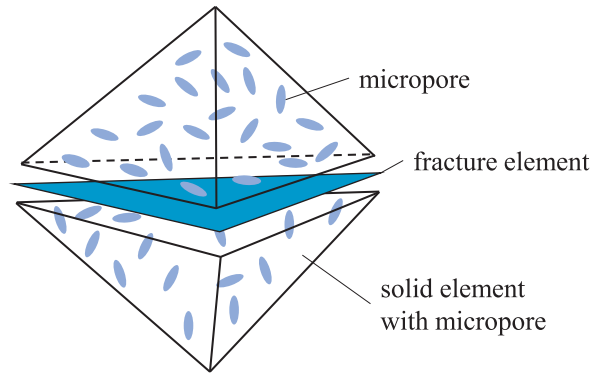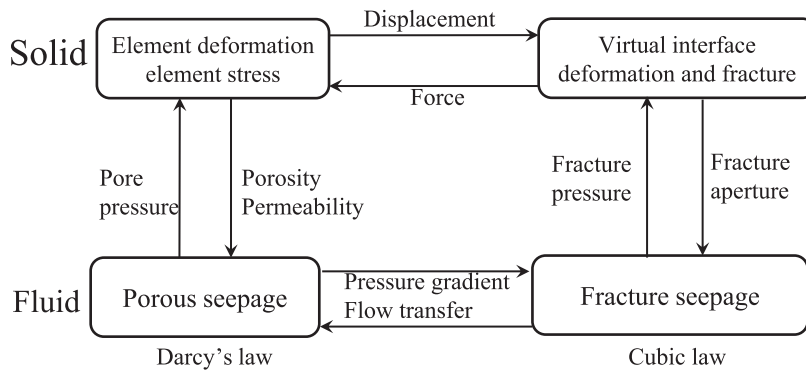
Fig. 2. Mesh configuration in the CDEM–HF3D.

Fig. 3. The coupling idea of the CDEM–HF3D.

3.2. Basic assumption

The CDEM–HF3D proposed in this paper should be subject to the following assumptions:

- The permeability of the rock blocks is characterized by the pore seepage, which obeys Darcy's Law.
- The permeability of fractures or joints is characterized by the fracture seepage, which obeys the cubic law.

The coupling idea of the CDEM–HF3D is shown in Fig. 3. The solution of the solid part is described in Section 2 and will not be repeated here. The following describes the calculation of pore seepage, fracture seepage and its coupling with the solid part.

3.3. Pore seepage model

In the calculation of pore seepage field, the material is assumed to be isotropic. Finite volume method (FVM) [43–48] is used to calculate the pore seepage field.

Based on Darcy's law, the fluid velocity of a node can be expressed as

$$v_i = k^E k_s \frac{\partial P^E}{\partial x_i}, \tag{6}$$

where x_i represents the coordinate component of the direction i of a node, and k_s represents the relative permeability coefficient, which is a function of average saturation $\overline{s^E}$

$$k_s = \overline{s^E}^2 (3 - 2\overline{s^E}), \tag{7}$$

where $k^E = \frac{\kappa}{\mu}$, and $\overline{s^E} = \sum_{i=1}^{N} s_i^E$, N is the total number of nodes of the pore element.

According to the Gaussian divergence theorem, Eq. (6) can be expressed as

$$v_i = k^E k_s \frac{1}{V} \sum_{j=1}^{M} \overline{P_j} n_i \Delta S_j, \tag{8}$$

where M is the total number of faces per pore element, V represents the element volume, n_i represents the component of the j_{th} face associated with the node in the direction i, $\overline{P_j}$ represents the average value of the total pressure P^E of the node in the j_{th} face, and ΔS_j is the j_{th} face area.

Based on the flow velocity (Eq. (8)), the flow rate of each node can be calculated

$$q = \sum_{j=1}^{M} (\boldsymbol{v} \cdot \boldsymbol{n}_j) \Delta S_j / N_j, \tag{9}$$

where $\boldsymbol{v}$ is the fluid velocity vector of pore element, $\boldsymbol{n}_j$ is the unit outer normal vector of j_{th} face, N_j is the total number of nodes of the j_{th} face. Then The total flow rate of node can be given by

$$Q^E = \sum_{j=1}^{N_e} q_j, \tag{10}$$

where N_e represents the number of elements connected to this node.

The saturation s^E of node can be calculated by node flow (Eq. (10))

$$s^E = -\sum_{t=0}^{t} \left(\frac{Q^E + Q_{app}}{nV} \Delta t \right), \tag{11}$$

where Q_{app} is the external flow boundary condition.

When the node saturation accumulates to 1, the fluid pressure p_p can be calculated according to Eqs. (10) to (11)

$$p_p = -\sum_{t=0}^{t} \left(k^E \frac{(Q^E + Q_{app})}{nV} \Delta t \right). \tag{12}$$

Then the total node pressure can be expressed as

$$P^E = p_p - \overline{s^E} \rho_e (x g_x + y g_y + z g_z), \tag{13}$$

where ρ_e represents the fluid density, g_x, g_y, g_z are the global component of the acceleration of gravity, respectively, x, y, z represent the three components of the global coordinate of a node, respectively, and $\overline{s^E}$ represents the average saturation of pore element $\overline{s^E} = \sum_{i=1}^{NE} s_i^E$.

The flow chart of pure pore seepage calculation as shown in Fig. 4.

3.4. Fracture seepage model

As shown in Fig. 5, fracture pressure and saturation are located at the node, and flow rate is located at the element centroid.

The calculation of fracture seepage is similar to that of pore seepage, except that the permeability coefficient k^F which is obtained here

$$k^F = \frac{w^2}{12\mu}. \tag{14}$$

3.5. Coupling algorithm of fracture–pore seepage

As shown in Fig. 6(a), we assume that the node of fracture element is F_i ($i = 1, 2, 3$), and the node of pore element is E_i ($i = 1, 2, 3$). The average saturation of the fracture element can be obtained by the node saturation
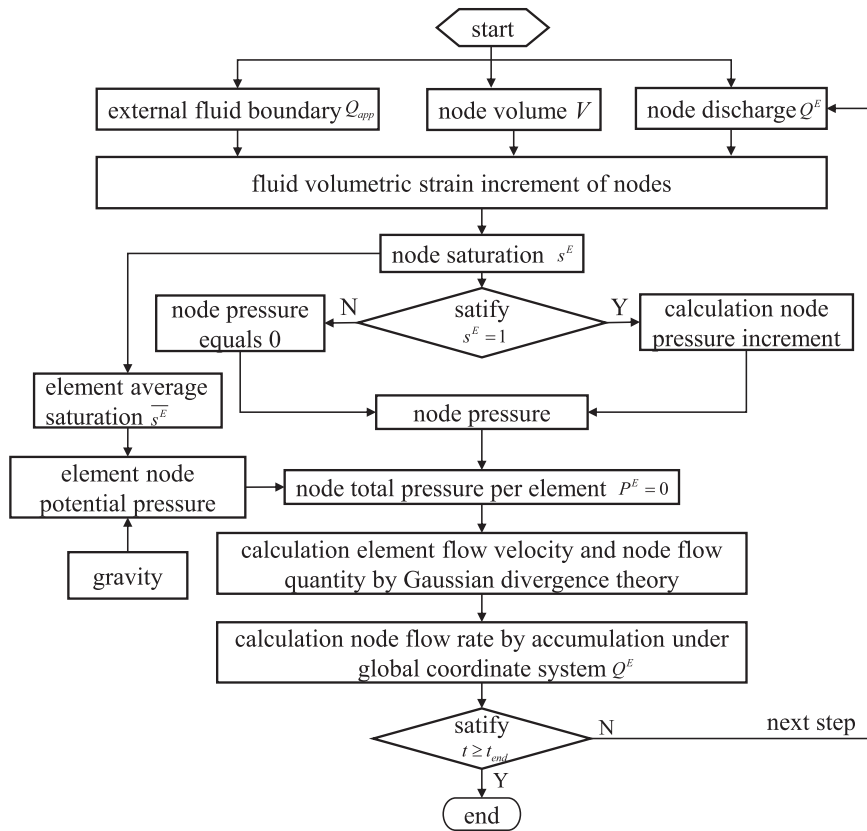
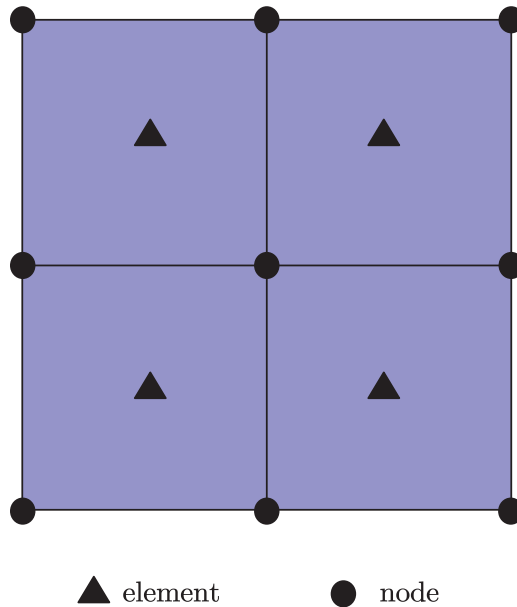**Fig. 4.** Flow chart of pure pore seepage calculation.

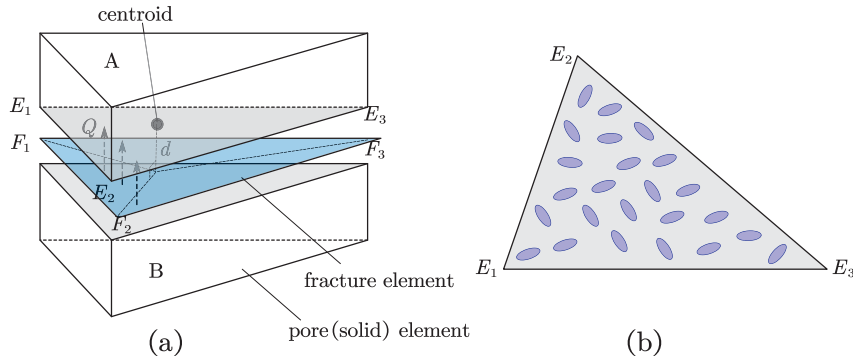**Fig. 5.** Schematic diagram of 2D planar fracture elements.

Fig. 6. The diagram of fracture–pore seepage coupling algorithm: (a) flow transfer between fracture and pore element, (b) pore cross-section on the coupling surface of fracture and pore.

over the element

$$\overline{s^F} = \sum_{i=1}^{N^F} \frac{s_i^F}{N^F}. \tag{15}$$

Based on the average saturation $\overline{s^F}$, the average pressure of the fracture element can be calculated

$$\overline{P^F} = \begin{cases} \sum_{i=1}^{N^F} \frac{P_i^F}{N^F}, & \overline{s^F} = 1, \\ 0, & \overline{s^F} < 1. \end{cases} \tag{16}$$

Similarly, the average pore element saturation can be given by the node saturation over the element

$$\overline{s^E} = \sum_{i=1}^{N^E} \frac{s_i^E}{N^E}. \tag{17}$$

Based on average saturation $\overline{s^E}$, the average pore element pressure can be expressed as

$$\overline{P^E} = \begin{cases} \sum_{i=1}^{N^E} \frac{P_i^E}{N^E}, & \overline{s^E} = 1, \\ 0, & \overline{s^E} < 1. \end{cases} \tag{18}$$

According to the Darcy's law, the flow velocity between fracture and pore can be expressed as

$$v = -k^E \frac{\overline{P^E} - \overline{P^F}}{d}, \tag{19}$$

where d is the vertical distance between the centroid of pore element and surface of fracture element (Fig. 6(a)).

In the coupling algorithm of fracture–pore seepage, the discharge of pore element can be expressed as $Q^E = vA$, then the discharge is uniformly distributed to the node of pore element face that coincide with the fracture element, which can be expressed as

$$Q_i^{EC} = Q^E / N_C^E, \tag{20}$$

where Q_i^{EC} represents the flow rate allocated to the i_{th} node on the coupling surface (Fig. 6(b)), and N_C^E represents the number of nodes on the coupling surface.

The flow rate of fracture element can be also given by $Q^F = vmA$, then the discharge is uniformly distributed to the node of fracture element face that coincide with the pore element, which can be expressed as

$$Q_i^{FC} = Q^F / N_C^F, \tag{21}$$

where m is the proportion of the area of the flow pipe on the coupling surface of fracture and pore element, we can think of it roughly as $m = n^{2/3}$. Q_i^{FC} represents the flow rate allocated to the i_{th} node of fracture element on the coupling surface, and N_C^F represents the number of nodes on the coupling surface, and $N_C^E = N_C^F$.
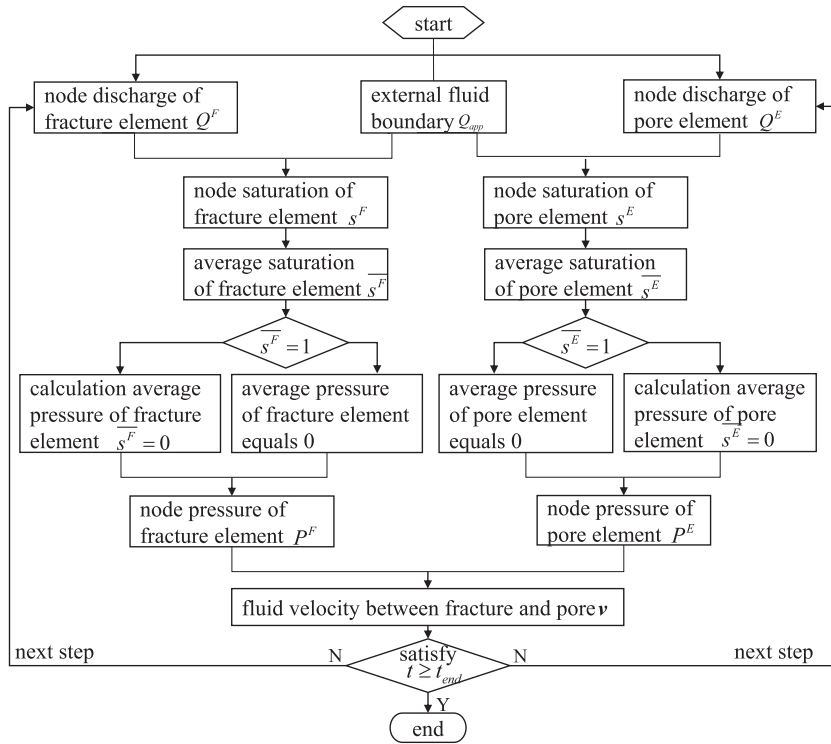
Fig. 7. Flow chart of fracture–pore seepage coupling algorithm.

The flow chart of fracture–pore seepage coupling algorithm as shown in Fig. 7.

3.6. Coupling algorithm of solid–pore seepage

The coupling algorithm of solid–pore seepage can be divided into full coupling, iterative coupling and pseudo-coupling. Among them, the stress field and seepage field in iterative coupling are calculated separately, that is, the stress field and pore seepage field are calculated respectively at each step, and then the corresponding data are exchanged to update the pore seepage field and stress field. In this paper, iterative coupling is selected as the solution method of the solid–pore seepage coupling algorithm.

When considering the influence of pore seepage on stress field, according to the principle of effective stress, the following formula is calculated

$$\sigma_{ij} = \sigma_{ij}^e - \alpha P^E, \tag{22}$$

where σ_{ij}^e is the effective stress of solid element and α is Biot coefficient.

When considering the influence of stress on pore seepage field, the porosity of rock matrix can be calculated according to the following formula

$$n = n_0 + \alpha\theta, \tag{23}$$

where n_0 represents the initial porosity, θ is the solid element volumetric strain.

The coupling algorithm of solid–pore seepage is shown in Fig. 8.

3.7. Coupling algorithm of solid–fracture seepage

The fluid flow in fracture element will apply fracture pressure on the two solid elements connected by the fracture element. Then the two solid elements will separate or close under the effect of the fracture pressure and external
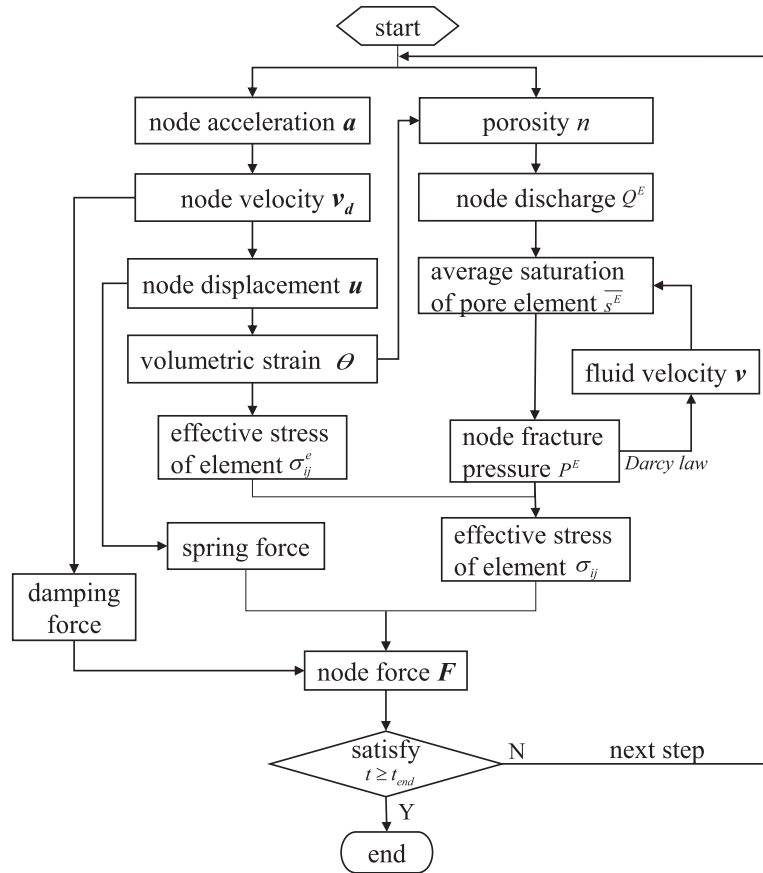
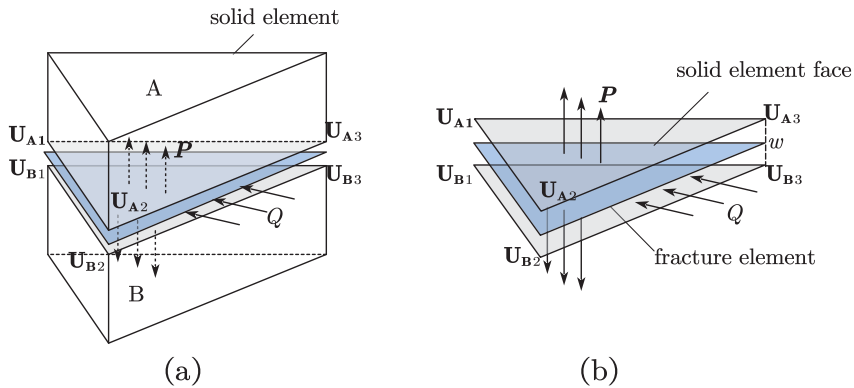**Fig. 8.** Flow chart of solid–pore seepage coupling algorithm.

Fig. 9. The diagram of solid–fracture seepage coupling algorithm.

load. The change of the relative displacement of the two solid elements will affect the opening degree of the fracture element. According to the cubic law, the fracture pressure will change with the change of fracture aperture.

As shown in Fig. 9, assume that we have known the flow rate Q^F of each node of fracture element, the fluid pressure P^F of each node can be given by Eqs. (12) and (13). Then the updated node displacement ($\mathbf{U}_{Ai}, \mathbf{U}_{Bi}, i = 1, 2, 3$) of solid elements can be obtained by putting the fluid pressure P^F into Eq. (1) to calculate the solid stress field and discontinuum field. The fracture aperture w can be calculated by

$$w_i = |\mathbf{U}_{Ai} - \mathbf{U}_{Bi}|, i = 1, 2, 3, \tag{24}$$

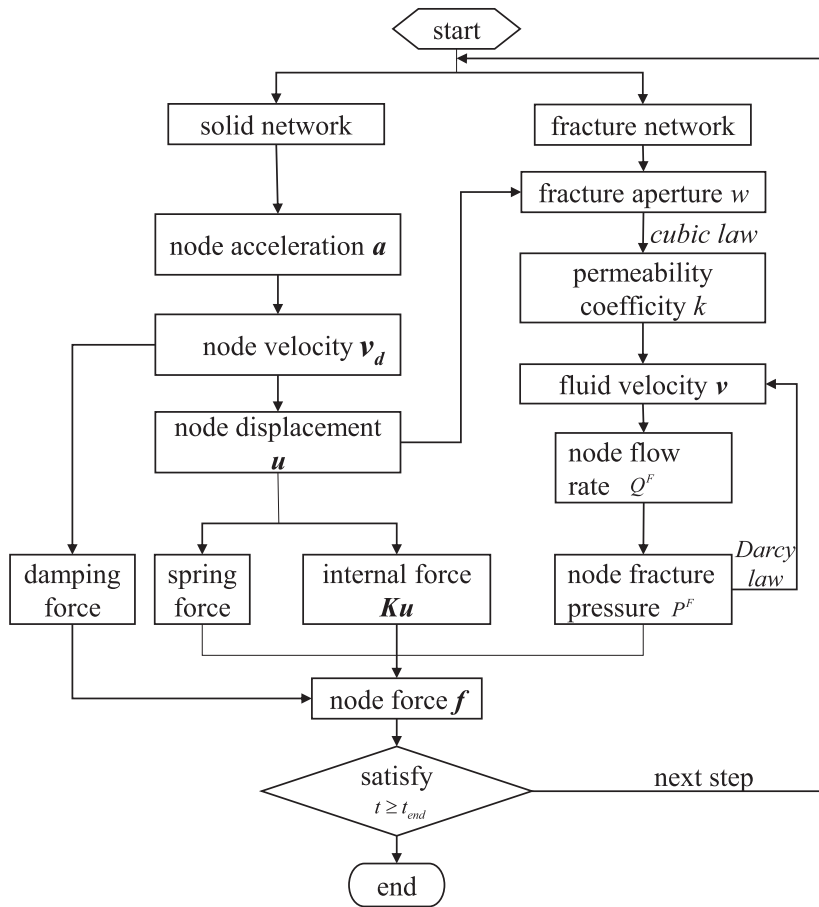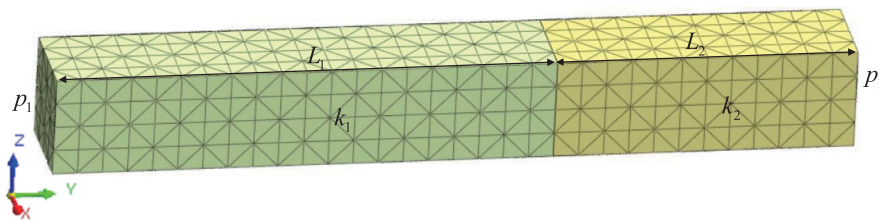**Fig. 10.** Flow chart of solid–fracture seepage coupling algorithm.

Fig. 11. Unidirectional flow in two different permeability formations.

where $\mathbf{U}_{Ai}$ is the coordinate vector of the top surface three nodes in solid element A, while $\mathbf{U}_{Bi}$ is the coordinate vector of the bottom surface three nodes in solid element B. Similar to the above, the fluid pressure P^F can be updated by Eqs. (12) and (13).

The coupling algorithm of solid–fracture seepage is shown in Fig. 10.

4. Examples

4.1. Pore seepage: Unidirectional flow in two different permeability formations

As shown in Fig. 11, the model which were divided into two sections according to different permeability coefficients was meshed into 2457 tetrahedral elements with an average size of 0.25 m. The left segment length is $L_1 = 5$ m, while the right segment length is $L_2 = 3$ m.
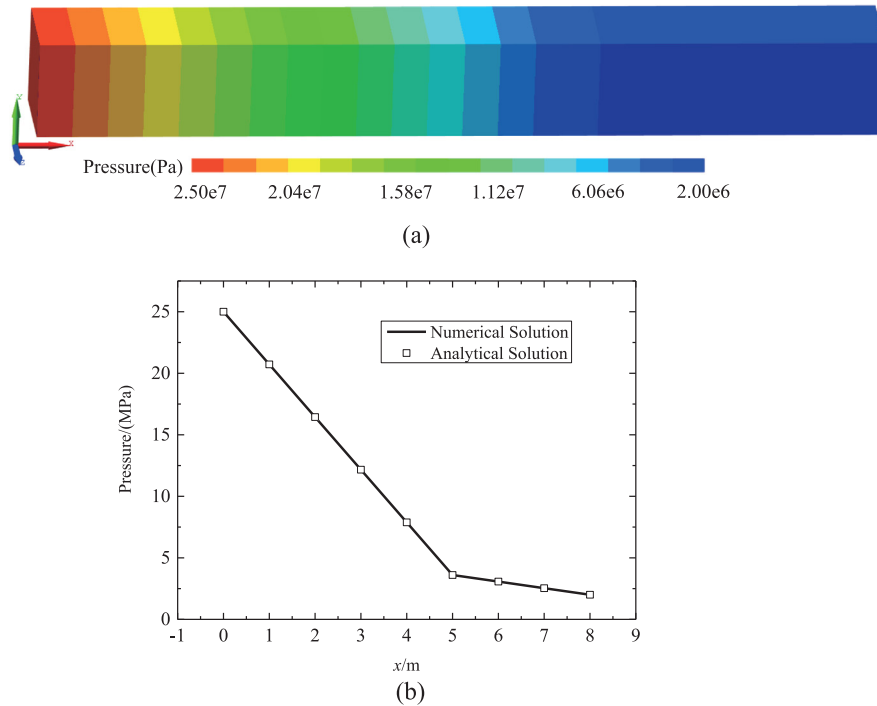
(a)

(b)

Fig. 12. Comparison of the numerical solution and the analytical solution of the fluid pressure distribution: (a) fluid pressure distribution in different permeability formations, (b) solution and analytical solution of the fluid pressure distribution along the x-axis direction.

The permeability of segment L_1 is $k_1 = 9.804 \times 10^{-15}$ m²/(Pa s), while at segment L_2 the permeability is $k_2 = 7.84 \times 10^{-14}$ m²/(Pa s). The fluid pressure on the left boundary surface is constant at $p_1 = 25$ MPa, and that on the right boundary surface is constant at $p_2 = 2$ MPa. The fluid bulk modulus $K = 2.2 \times 10^9$ Pa, and fluid viscosity coefficient $\mu = 1$ Pa s. This is a pure pore seepage problem, not involving mechanical calculation, and the time step of numerical calculation is 10 s. The relationship between the fluid pressure and the spatial position in the length direction can be expressed as follows [49]

$$
p = \begin{cases} p_1 - \dfrac{p_1 - p_2}{k_1(\dfrac{L_1}{k_1} + \dfrac{L_2}{k_2})}x, & 0 < x < L_1, \\[4mm] \dfrac{k_1 L_2 p_1 + k_2 L_1 p_2}{k_1 L_2 + k_2 L_1}L_1 + \dfrac{p_1 - p_2}{k_2(\dfrac{L_1}{k_1} + \dfrac{L_2}{k_2})}(L_1 - x), & L_1 < x < L_1 + L_2. \end{cases}
\tag{25}
$$

The final fluid pressure obtained by the CDEM–HF3D as shown in Fig. 12. The fluid pressure decreases from left to right, and the fluid pressure in the left segment L_1 drops more quickly than that in the right segment L_2 (Fig. 12(a)). As shown in Fig. 12(b), the fluid pressure curve along the x-axis is piecewise linear distribution, with the turning point along x-axis at $x = 5$ m. The pressure gradient in the left segment is larger than that in the right segment. The numerical solution of the fluid pressure along the x-axis is in good agreement with the analytical solution.

4.2. Fracture seepage: Unidirectional unsaturated seepage

As shown in Fig. 13, it is assumed that a horizontal fracture is 100 m long, 1 m wide and 1 m high respectively. The initial opening of the fracture is 0.1 mm, the fluid viscosity coefficient $\mu = 0.83$ Pa s, and the vacuum is inside

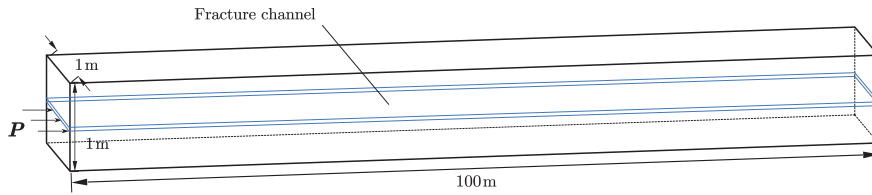**Fig. 13.** The geometry model of Unidirectional unsaturated seepage.
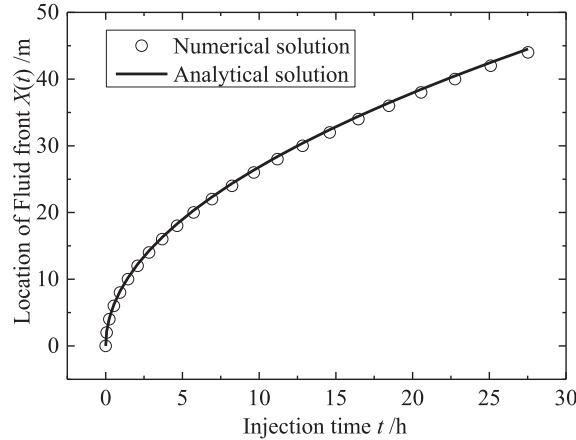

Fig. 14. Sharp front position vs. seepage time.

the fracture. The injection pressure on the left side of the model is 10 MPa, the fluid density is 1000 kg/m^3, and the fluid volumetric modulus is 200 MPa.

There is an analytical solution for this example. The relationship between the location of fluid front and the seepage time under vacuum can be expressed as [50]

$$X(t) = \sqrt{2k P_0 t}, \tag{26}$$

where k represents the fracture permeability coefficient, P_0 is the fluid injection pressure, and t is the seepage time.

The comparison curve between the solution of CDEM–HF3D and the theoretical solution is shown in Fig. 14. It can be seen from the figure that the numerical solution is basically the same as the analytical solution, which shows the accuracy of CDEM–HF3D in solving the unstable front peak line.

4.3. Solid–pore seepage: Mandel–Cryer problem

As shown in Fig. 15, the model is a sphere with a radius of 0.1 m. Considering symmetry, 1/8 of the sphere is taken as the object of study. The model was meshed into 40,561 tetrahedral elements. In the calculation of solid stress field, normal constraints were applied to the left and bottom of the model. The model with a density of $\rho_d = 2500$ kg/m^3, a Young's modulus of $E = 1$ MPa, a Poisson's ratio of $\nu = 0.25$, and local damping is 0.8. In calculation of pore seepage field, the impermeable boundary is set at the left and bottom of the model, and the fluid pressure at the outer sphere is fixed at 0, the initial pore pressure of the whole model is 100 kPa (effective solid stress is 0). The density of water is $\rho_w = 1000$ kg/m^3, the porosity is $n = 0.1$, compression modulus is $M = 1$ MPa, the permeability coefficient is $k = 1 \times 10^{-8}$ m^2/(Pa s), and the Biot coefficient is 1.0.

In the Mandel–Cryer problem, the theoretical solution of the pressure time history at the center of the sphere can be expressed as [51]

$$\frac{p(t)}{P_0} = \sum_{n=1}^{\infty} \frac{8\eta(\sqrt{x_n} - sin\sqrt{x_n})}{(x_n - 12\eta + 16\eta^2)sin\sqrt{x_n}} e^{-x_n t^*}, \tag{27}$$
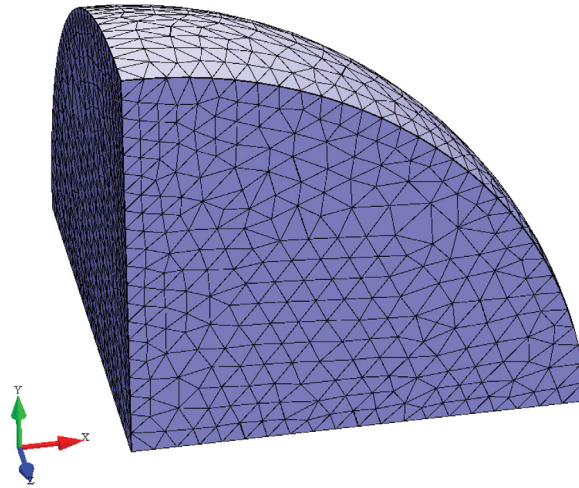
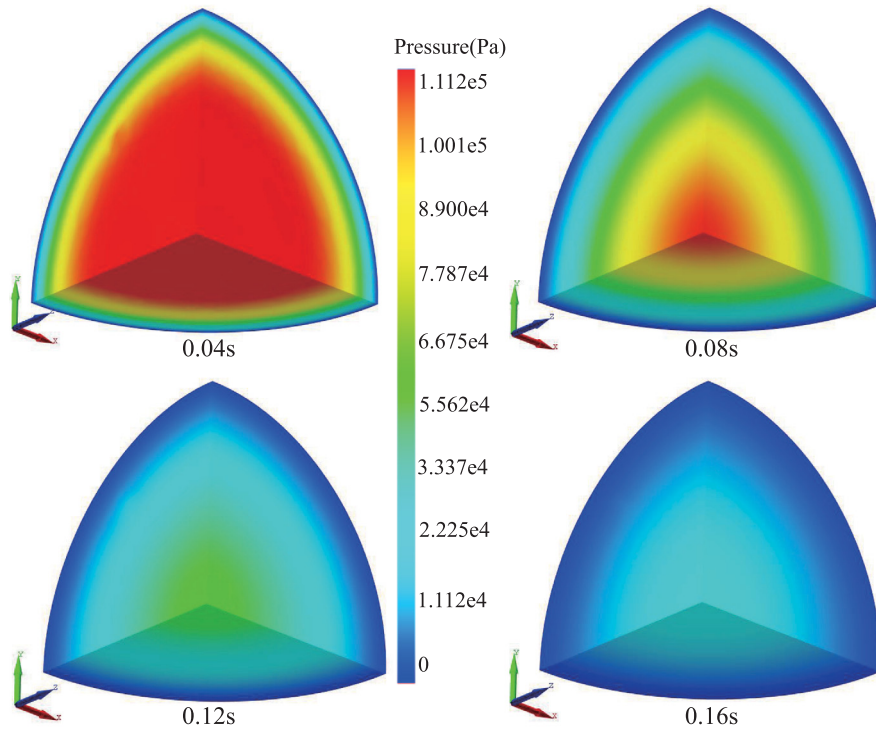**Fig. 15.** The numerical model of Mandel–Cryer problem.

Fig. 16. Evolution of pore pressure distribution.

where P_0 is the initial pore pressure of the entire model, $\eta = \dfrac{1-2\nu}{2(1-\nu)}$ is the pore elastic stress coefficient, ν is Poisson's ratio, and $t^* = \dfrac{ct}{R_0^2}$ is dimensionless time.

The evolution of the pore pressure distribution in the model is shown in Fig. 16. The pressure time history data at the center point of the sphere was recorded and compared with the analytical solution, as shown in Fig. 17. At the beginning of the calculation, the pore pressure showed an upward trend, and reached the maximum peak pressure (130 kPa) at $t = 0.05$ s, then decreased slowly and tended to be stable. The early jump of pore pressure is caused
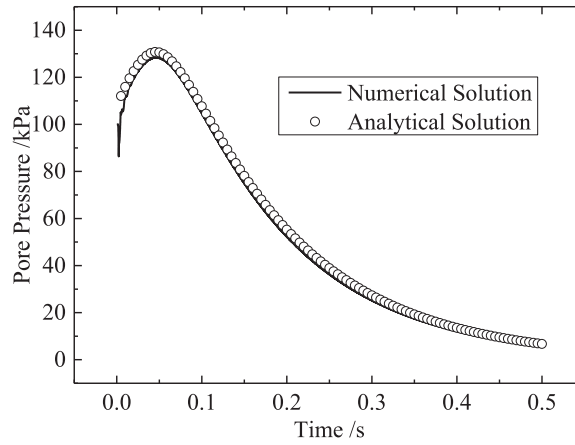
Fig. 17. Pore pressure time history curve at the center of the sphere.

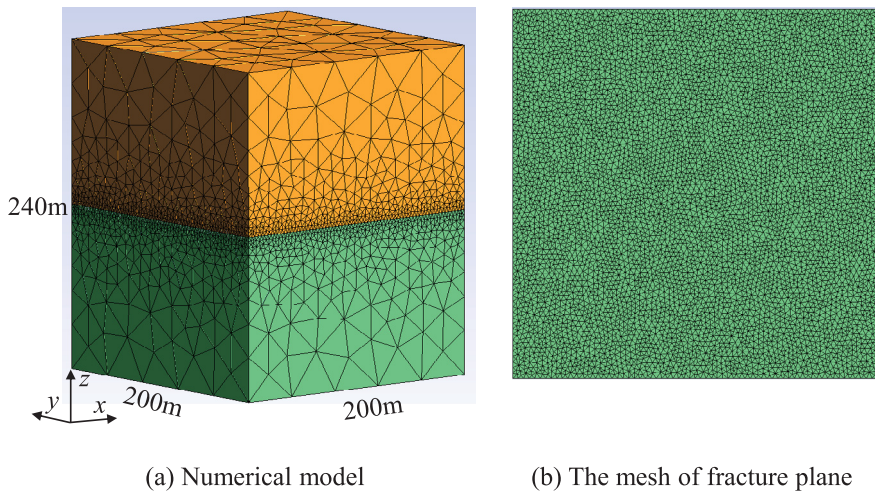(a) Numerical model   (b) The mesh of fracture plane

Fig. 18. The numerical model of radial hydraulic fracture.

by the elastic unloading after the surface pore pressure is set to 0. In general, the pore pressure of the numerical solution is slightly lower than that of the analytical solution, but the overall trend is consistent and the agreement is good.

4.4. Radial hydraulic fracture with CDEM–HF3D

As shown in Fig. 18, the model was meshed into 79,657 tetrahedral elements and the element size in the fracture plane is 3 m. Initial compressive stress of the whole model is taken as 20 MPa, while the pore pressure is 10 MPa. According to [52], the scaled material parameters were introduced as

$$\mu' = 12\mu, \ E' = \frac{E}{1 - \nu^2}, \ K' = 4(\frac{2}{\pi})^{0.5}K_{Ic}. \tag{28}$$

For the viscosity dominated regime, the parameters are $\mu' = 0.2$ Pa s, $E' = 20 \times 10^9$ Pa, $K' = 3 \times 10^6$ Pa m$^{1/2}$. What is more, the injection rate at the center of fracture plane $Q_0 = 0.01$ m^3/s, and the injection time $t = 1000$ s. Then the tension strength for each spring of interface model can be deduced by $\sigma_t = a\frac{K_{Ic}}{d^{1/2}}$[53], where d is the average element size of fracture plane, a is a numeric parameter which assumed equal to 1 in this paper.

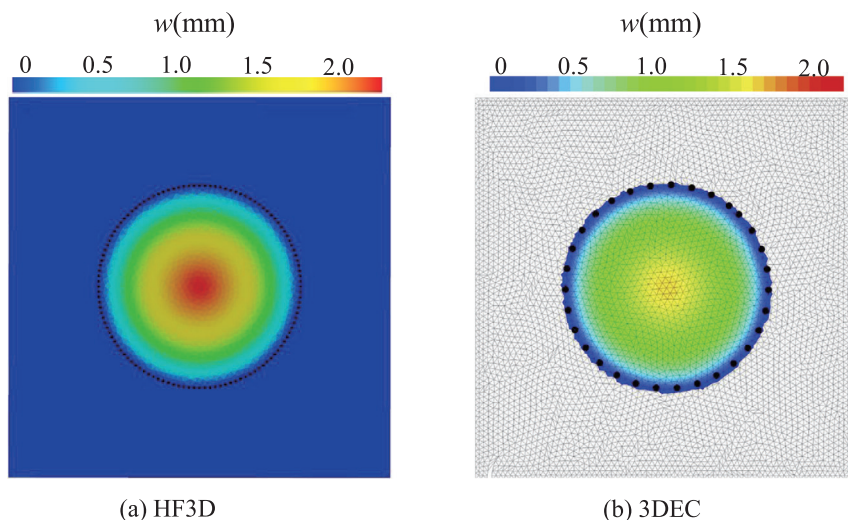(a) HF3D   (b) 3DEC

Fig. 19. The fracture aperture contours of radial hydraulic fracture: (a) the result of HF3D, (b) the result of 3DEC [52]. The dotted lines indicate the footprint of the radial fracture solution.
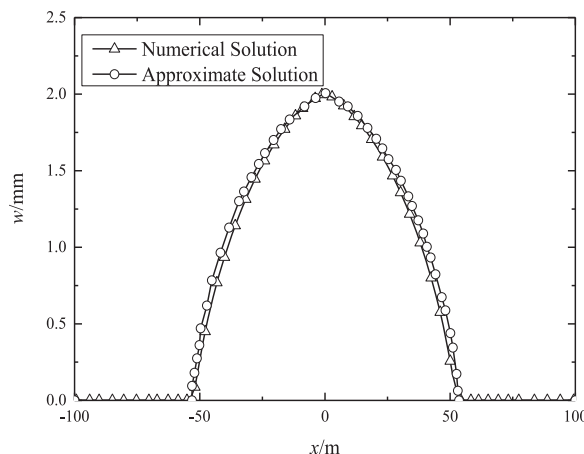

Fig. 20. Comparison of fracture aperture variation along the horizontal axis with approximate results [54] at $t = 1000$ s.

The fracture aperture contours of numerical simulation are shown in Fig. 19. And the solution of radial hydraulic fracture is shown in Fig. 20. Compared with the approximate solution, the propagation radius of the fracture is 52.87 m, the error is 0.4%, and the maximum aperture is 2.02 mm, the maximum error is 1.0%. Results demonstrate that the HF3D model is able to predict accurately fracture size.

4.5. Solid–fracture seepage: Hydraulic fracturing of laminated shale formation

The geometric and numerical model of layered shale as shown in Fig. 21 was established. According to the Ref. [55], the model was cut into 30 cm × 30 cm × 30 cm, the compressive strength $\sigma_c = 103.78$ MPa, the elastic modulus $E = 32.44$ GPa, and the Poisson's ratio $v = 0.23$. The material parameters of the bedding planes in the laminated shale formation are not given in the reference. Here, we assume that the tensile strength of bedding planes are $T = 3$ MPa, and the internal friction angle is $\phi = 30°$.

In the simulation, the in-situ stress state of the model is satisfied with the condition of strike slip faulting ($\sigma_H = 25$ MPa, $\sigma_V = 18$ MPa, $\sigma_h = 6$ MPa (Fig. 21a)), where the maximum and minimum horizontal stresses σ_H, σ_h along the direction of bedding planes, and the vertical stress σ_V perpendicular to the bedding plane. In order
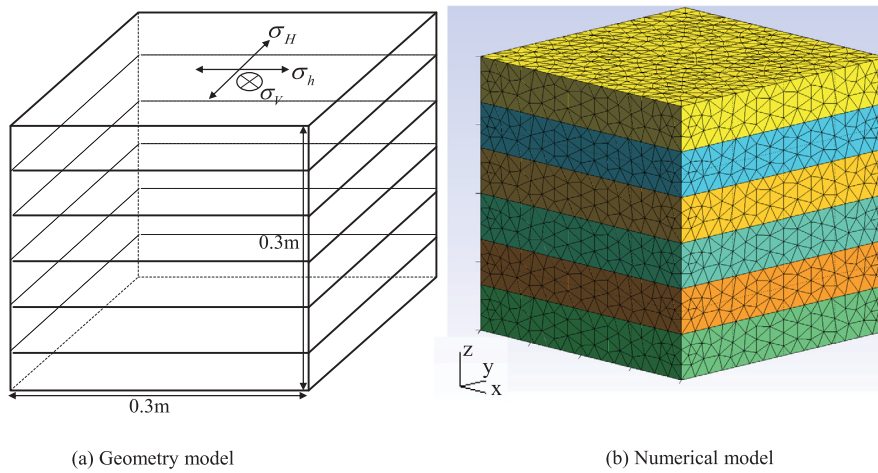
(a) Geometry model (b) Numerical model

Fig. 21. Geometric and numerical model of layered shale: (a) geometric model, (b) numerical model.
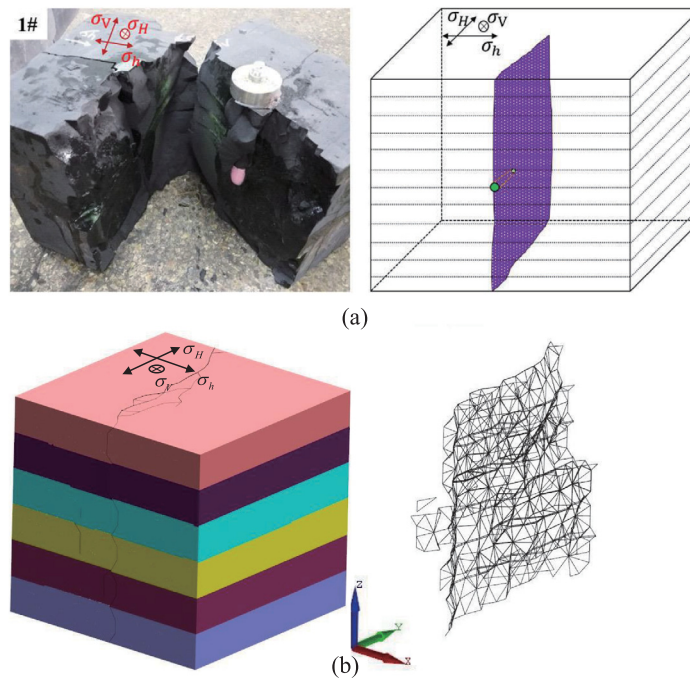

Fig. 22. Hydraulic fracture morphology after fracturing: (a) experimental result [55], (b) numerical result.

to be consistent with the test loading sequence described in Ref. [55], the following sequence loading is adopted in the numerical simulation: Firstly, the minimum horizontal stress of 6 MPa is respectively loaded in three directions at the same time to be solved to stability; Secondly, another loading 12 MPa is respectively loaded in the maximum horizontal direction and vertical direction at the same time to be solved to stability; Thirdly, another loading 7 MPa is loaded in maximum horizontal direction, and solve it until is stable; Finally, the water pressure at the center of the model was applied with a constant flow rate of 60 mL/min.

As shown in Fig. 22, the right side of each picture shows an illustration of fracture network in the laminated shale. Fig. 22(a) is the experimental result and Fig. 22(b) is the numerical result. Under the influence of the current in-situ stress and hydraulic fracturing, a single fracture network which is nearly perpendicular to the bedding planes
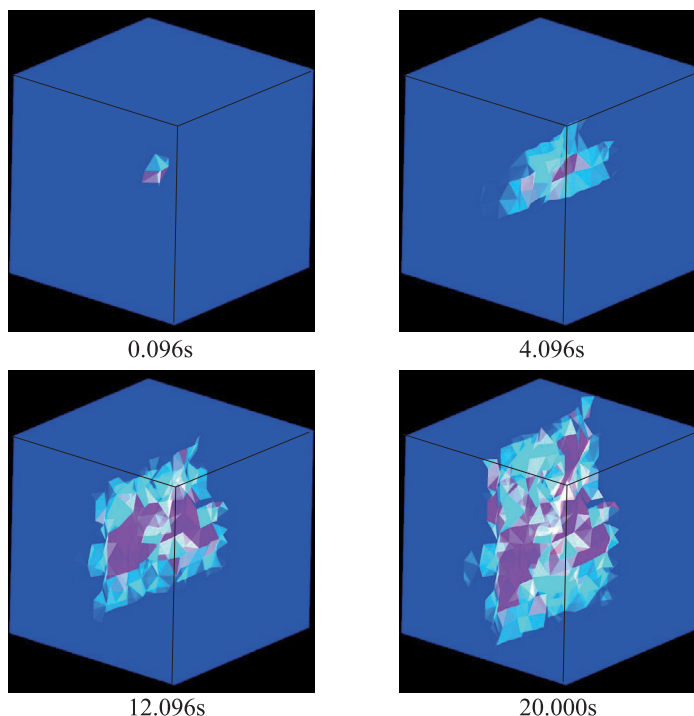
Fig. 23. The evolution of hydraulic fracture morphology.

appears in the laminated shale. By comparing with the experimental results, it can be intuitively seen that the fracture morphology of them are basically the same, which also verifies the accuracy of the CDEM–HF3D.

The dynamic evolution of cracks in the laminated shale from initiation, propagation to transfixion is shown in Fig. 23. At the initial moment ($t = 0.096$ s), the cracks originate in the central position of the laminated shale, and then propagation in all directions on the plane perpendicular to the bedding plane. During this period (before $t = 20$ s), the propagation speed of cracks along the bedding plane is greater than that perpendicular to the bedding plane. Finally, with the continuous injection of the flow rate, the cracks penetrates the whole laminated shale.

Four monitoring points (A1, A2, A3, A4) were arranged on the fracture network and A1 was located at the injection hole, in Fig. 24. According to the pressure curve, the closer the position is to the injection hole, the larger the peak pressure is, and the maximum peak pressure is 66 MPa (point A1 at $t = 0.2$ s). Then the pressure of points began to drop after reaching the peak pressure, and the closer to the injection hole, the greater the pressure drop gradient is.

4.6. Solid–pore–fracture seepage: Hydraulic fracturing of a disk with one injection hole

Fig. 25 shows a disk with a radius of 5.0 m and a thickness of 0.3 m. There is an injection hole with a radius of 0.5 m at the center of the disk. The entire model was meshed into 7776 wedge elements with size of 0.25 m. The material parameter of the model is density $\rho_d = 2600$ kg/m^3, elastic modulus $E = 55$ GPa, Poisson's ratio $v = 0.25$, tensile strength $T = 2.5$ MPa. The fluid pressure at the injection hole is fixed at 3.0 MPa, while the outer boundary surface of the disk is free. The bulk modulus of the fluid $K = 2.2$ GPa, the viscosity coefficient of the fluid $\mu = 1$ Pa s, the fluid density $\rho_w = 1000$ kg/m^3, and the initial fracture opening is 5×10^{-5} m.

Fig. 26 shows the fluid pressure distribution at different moments under hydraulic fracturing (fracture pressure on the left side and pore pressure on the right side). We can see that the propagation velocity of cracks is ahead of the velocity of seepage pressure during the whole fracturing process, which is related to the interface strength. With the emergence of cracks, the fracture pressure increases significantly along the crack propagation direction and exhibits four radial distributions. This is because the newly generated cracks make the hydraulic aperture of fracture elements
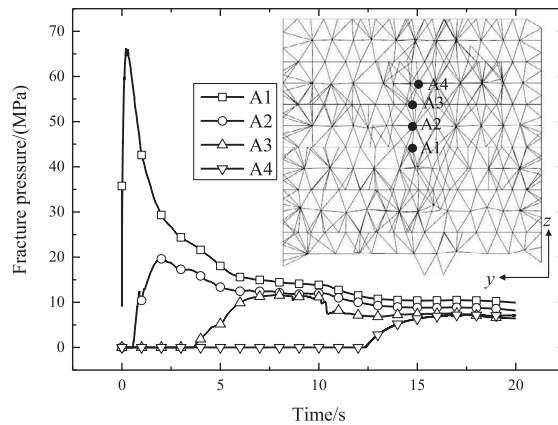
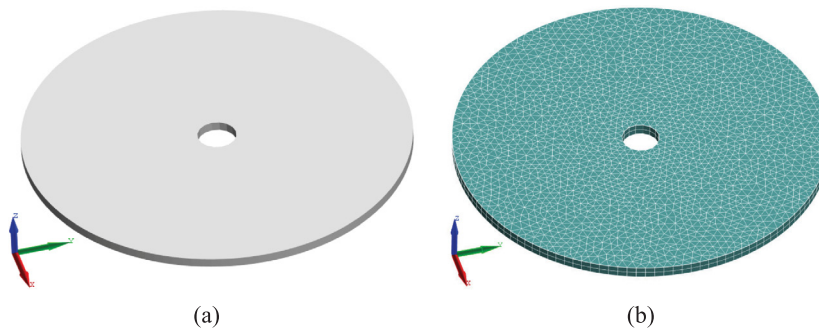**Fig. 24.** The time history curve of fracture pressure.

Fig. 25. Geometric and numerical model of a disk: (a) geometric model, (b) numerical model.

significantly increase, and the fluid flows more easily along the fracture channel. With the increase of seepage time, the pore pressure also begins to increase gradually behind the fracture pressure because of the permeability of the rock matrix. And fluid can flow into the rock matrix through solid elements with micropores on both sides of the fracture elements.

To further analyze the variation of the fluid pressure, three monitoring points are set as shown in Fig. 27(a). A1–A3 are all located on the boundary of the newly generated cracks, where point A1 is located on a circumference with a radius of 0.74 m, point A2 is located on a circumference with a radius of 1.59 m, and point A3 is located on a circumference with a radius of 2.22 m. We observe the variation of fracture pressure and pore pressure at those monitoring points during hydraulic fracturing. As shown in Fig. 27(b), the fracture pressure of point A1 starts to increase gradually at $t = 0.013$ s because the saturation of fracture elements reaches 1, then the fracture pressure of point A2 and point A3 also starts to increase gradually at $t = 0.069$ s and $t = 0.108$ s, respectively. The fracture pressure of the three points has the same growth trend and fluctuate with seepage time, which reflects the initiation, growth and propagation process of the cracks. We can also find that the closer a point is to the injection hole, the larger the fracture pressure is at the same moment.

Similarly, for the pore pressure of the three points, the smaller the distance from the injection hole, the larger pressure is. And the pore pressure of point A3 is always zero because the fluid has not yet arrived during the hydraulic fracturing.

Next we analyze the pore pressure and fracture pressure at the same point. Take point A1 as an example, the fracture pressure is larger than the pore pressure. And the fracture pressure at point A1 gradually increases from zero when $t = 0.013$ s, while the pore pressure remains at zero until $t = 0.051$ s. This means that the saturation accumulation value of fracture elements has reached 1 during this period, whereas the saturation in the rock matrix has not reached 1 yet. After this period, the pore pressure starts to increase gradually from zero because the accumulation value of pore saturation reaches 1.
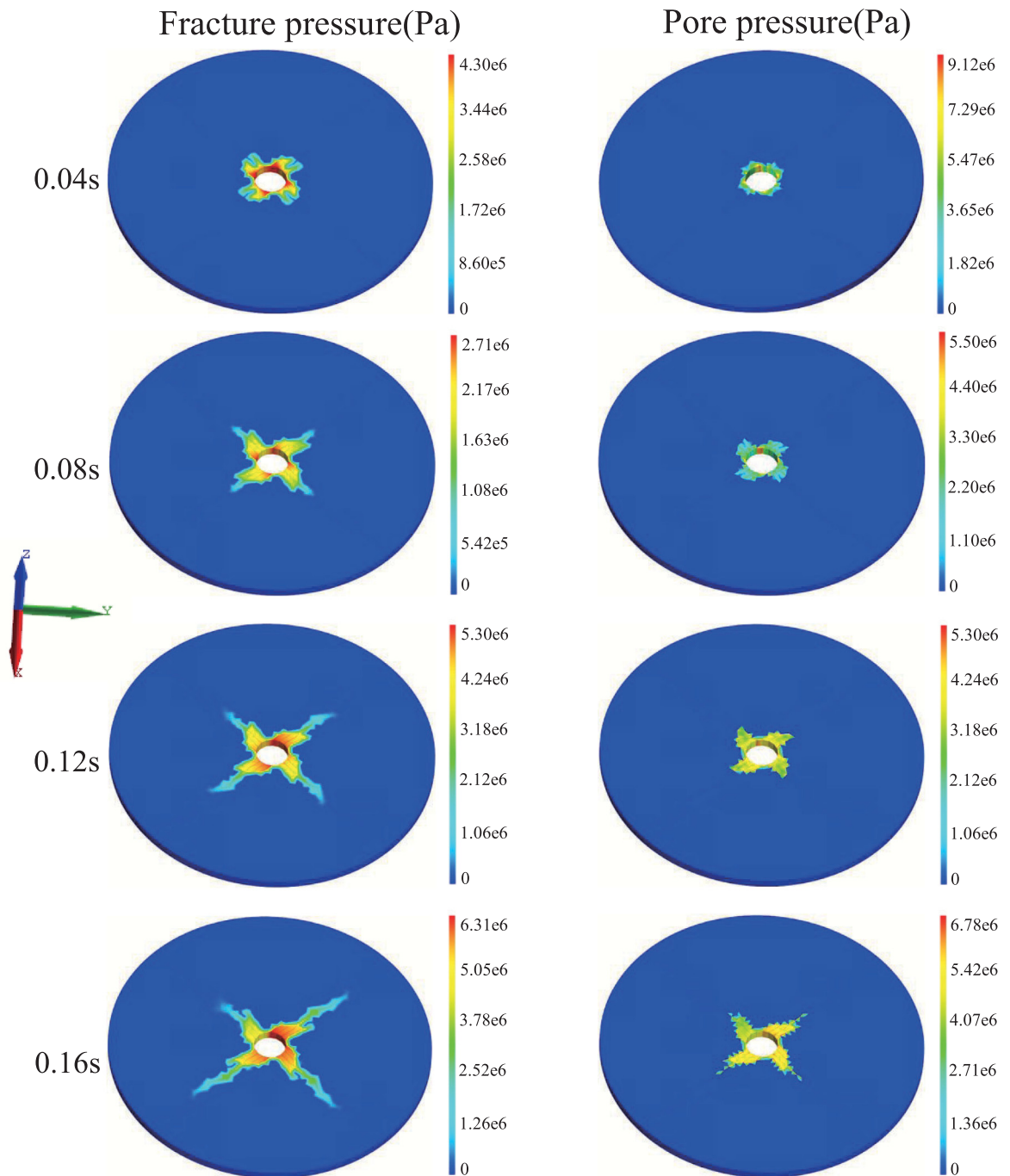
Fig. 26. Evolution of fluid pressure distribution and crack propagation during hydraulic fracturing.

By this example, it can be observed that the proposed CDEM–HF3D in this paper takes into account the permeability of both the micropores of rock matrix and fractures by considering the pore seepage and fracture seepage.

5. Conclusions

In this paper, a CDEM–HF3D model which can consider pore seepage, fracture seepage and crack propagation simultaneously for hydraulic fracturing is proposed. The following conclusions can be drawn:
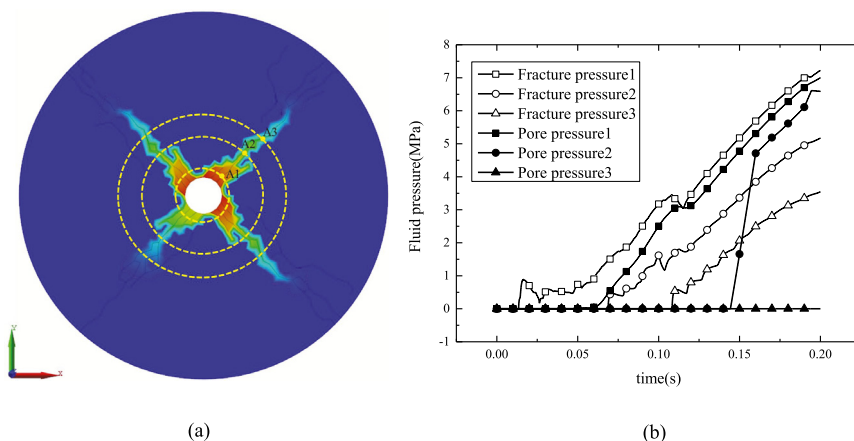
| (a) | (b) |

Fig. 27. The time history curves of some monitoring points: (a) locations of monitoring points, (b) the time history curves of fluid pressure.

(1) The coupled model which can simulate the whole process of cracks from initiation, propagation to intersection was established based on continuum–discontinuum element method. The advantages of this model are that it not only includes the fluid flow in joints or fractures, but also the fluid leak-off into the rock matrix from the fracture.

(2) The precision of the fracture seepage and pore seepage algorithms in the proposed model is verified by two samples with analytical solutions. And the validity of coupling algorithms such as solid–pore seepage, solid–fracture seepage are verified by a Mandel–Cryer problem, a radial hydraulic fracture and a hydraulic fracturing experiment.

(3) A hydraulic fracturing of a disk with one injection hole is simulated, in which the coupling of solid stress field, discontinuum field, pore seepage field and fracture seepage field is considered simultaneously. The result shows that the fluid can not only flow in fractures, but also infiltrate into the pore matrix of the rock mass, which can characterize the distribution of fluid pressure in the disk, including pore pressure and fracture pressure. In addition, the example also reveals the initiation, expansion and interlacing of cracks within the disk driven by fluid.

Through these examples, the reasonability and availability of the CDEM–HF3D proposed in this paper are demonstrated.

Declaration of competing interest

The authors declare that they have no known competing financial interests or personal relationships that could have appeared to influence the work reported in this paper.

Data availability statement

Data in this manuscript is good to offer, is there is any request, please contact Corresponding Author.

Acknowledgments

References

[1] B.H. Kazemi, L.S.M. Jr, K.L. Porterfield, P.R. Zeman, Numerical simulation of water-oil flow in naturally fractured reservoirs, Soc. Pet. Eng. J. 16 (6) (1976) 1114–1122.

[2] B. Shen, O. Stephansson, M. Rinne, H.S. Lee, L. Jing, K. Roshoff, A fracture propagation code and its applications to nuclear waste disposal, Int. J. Rock Mech. Min. Sci. 41 (3) (2004) 448–449.

[3] D. Blessent, R. Therrien, C.W. Gable, Large-scale numerical simulation of groundwater flow and solute transport in discretely-fractured crystalline bedrock, Adv. Water Resour. 34 (12) (2011) 1539–1552.

[4] M.A. Grant, Geothermal reservoir engineering, Eos Trans. Amer. Geophys. Union 64 (31) (2013) 486–486.

[5] W. Shen, Y. Xu, X. Li, W. Huang, J. Gu, Numerical simulation of gas and water flow mechanism in hydraulically fractured shale gas reservoirs, J. Natl. Gas Sci. Eng. 35 (2016) 726–735.

[6] K.T. Terzaghi, Theoretical soil mechanics, 1943.

[7] Biot, A. Maurice, General theory of three-dimensional consolidation, J. Appl. Phys. 12 (2) (1941) 155–164.

[8] M.A. Biot, Theory of elasticity and consolidation for a porous anisotropic solid, J. Appl. Phys. 26 (2) (1955) 182–185.

[9] T.K. Perkins, L.R. Kern, Widths of hydraulic fractures, J. Pet. Technol. 13 (9) (1961) 937–949.

[10] R.P. Nordgren, Propagation of a vertical hydraulic fracture, Soc. Pet. Eng. J. 12 (04) (1970) 306–314.

[11] J. Geertsma, F. De Klerk, A rapid method of predicting width and extent of hydraulically induced fractures, J. Pet. Technol. 21 (12) (1969) 1571–1581.

[12] E. Detournay, Propagation regimes of fluid-driven fractures in impermeable rocks, Int. J. Geomech. 4 (1) (2004) 35–45.

[13] E. Detournay, Propagation regimes of fluid-driven fractures in impermeable rocks, Int. J. Geomech. 4 (1) (2004) 35–45.

[14] A. Peirce, E. Detournay, An implicit level set method for modeling hydraulically driven fractures, Comput. Methods Appl. Mech. Engrg. 197 (2008) 2858–2885, http://dx.doi.org/10.1016/j.cma.2008.01.013.

[15] E.V. Dontsov, A.P. Peirce, An enhanced pseudo-3D model for hydraulic fracturing accounting for viscous height growth, non-local elasticity, and lateral toughness, Eng. Fract. Mech. 142 (2015) 116–139.

[16] J.I. Adachi, E. Detournay, A.P. Peirce, Analysis of the classical pseudo-3D model for hydraulic fracture with equilibrium height growth across stress barriers, Int. J. Rock Mech. Min. Sci. 47 (4) (2010) 625–639.

[17] A. Settari, M. Cleary, Development and testing of a pseudo-three-dimensional model of hydraulic fracture geometry (p3dh), in: Proceedings of the 6th SPE symposium on reservoir simulation of the Society of Petroleum Engineers, in: SPE 10505, vol. January-February, 1982, pp. 185–214.

[18] E. Siebrits, A.P. Peirce, An efficient multi-layer planar 3D fracture growth algorithm using a fixed mesh approach, Internat. J. Numer. Methods Engrg. 53 (3) (2010) 691–717.

[19] A.P. Bunger, E. Detournay, Early-time solution for a radial hydraulic fracture, J. Eng. Mech. 133 (5) (2007) 534–540.

[20] A.A. Savitski, E. Detournay, Propagation of a penny-shaped fluid-driven fracture in an impermeable rock: asymptotic solutions, Int. J. Solids Struct. 39 (26) (2002) 6311–6337.

[21] E.V. Dontsov, An approximate solution for a penny-shaped hydraulic fracture that accounts for fracture toughness, fluid viscosity and leak-off, R. Soc. Open Sci. 3 (12) (2016) 221–237.

[22] E. Detournay, Mechanics of hydraulic fractures, Annu. Rev. Fluid Mech. 48 (1) (2016) 311–339.

[23] S.L. Crouch, Boundary element methods in solid mechanics, with applications in rock mechanics and geological engineering. (metody granichnykh ehlementov v mekhanike tverdogo tela). (metody granichnykh ehlementov v mekhanike tverdogo tela.) transl. from the english., J. Appl. Mech. 50 (3) (1983) 704.

[24] A.P. Peirce, E. Siebrits, Uniform asymptotic approximations for accurate modeling of cracks in layered elastic media*, Int. J. Fract. 110 (3) (2001) 205–239.

[25] N. Nagel, M. Sanchez-Nagel, Stress Shadowing and Microseismic Events: A Numerical Evaluation, Vol. 5, 2011, pp. 4223–4243, http://dx.doi.org/10.2118/147363-ms, cited By 64.

[26] B. Lecampion, A. Bunger, X. Zhang, Numerical methods for hydraulic fracture propagation: A review of recent trends, J. Natl. Gas Sci. Eng. 49 (2018) 66–83.

[27] A. Taleghani, J. Olson, Analysis of multistranded hydraulic fracture propagation: An improved model for the interaction between induced and natural fractures, 2009.

[28] T. Mohammadnejad, A.R. Khoei, An extended finite element method for hydraulic fracture propagation in deformable porous media with the cohesive crack model, Finite Elem. Anal. Des. 73 (2013) 77–95.

[29] Yiming, Zhang, Roman, Lackner, Matthias, Zeiml, A. Herbert, Mang, Strong discontinuity embedded approach with standard SOS formulation: Element formulation, energy-based crack-tracking strategy, and validations, Comput. Methods Appl. Mech. Engrg. 287 (Apr.15) (2015) 335–366.

[30] Y. Zhang, X. Zhuang, Cracking elements: A self-propagating strong discontinuity embedded approach for quasi-brittle fracture, Finite Elem. Anal. Des. 144 (MAY) (2018) 84–100.

[31] Y. Zhang, Z. Gao, Y. Li, X. Zhuang, On the crack opening and energy dissipation in a continuum based disconnected crack model, Finite Elem. Anal. Des. 170 (2019) 103333.

[32] A. Peirce, E. Detournay, An implicit level set method for modeling hydraulically driven fractures, Comput. Methods Appl. Mech. Engrg. 197 (33) (2008) 2858–2885.

[33] E.V. Dontsov, A.P. Peirce, A multiscale implicit level set algorithm (ILSA) to model hydraulic fracture propagation incorporating combined viscous, toughness, and leak-off asymptotics, Comput. Methods Appl. Mech. Engrg. 313 (JAN.1) (2017) 53–84.

[34] B. Lecampion, E. Detournay, An implicit algorithm for the propagation of a hydraulic fracture with a fluid lag, Comput. Methods Appl. Mech. Eng. 196 (49–52) (2007) 4863–4880.

[35] M.J. Hunsweck, Y. Shen, A.J. Lew, A finite element approach to the simulation of hydraulic fractures with lag, Int. J. Numer. Anal. Methods Geomech. 37 (9) (2013).

[36] S. Salimzadeh, N. Khalili, A three-phase XFEM model for hydraulic fracturing with cohesive crack propagation, Comput. Geotech. 69 (sep.) (2015) 82–92.

[37] P.A. Cundall, A computer model for simulating progressive large-scale movements in blocky rock systems, Proc. Int. Symp. Rock Fract. 1 (ii-b) (1971) 11–18.

[38] Shi, Gen-Hua, Discontinuous deformation analysis: A new numerical model for the statics and dynamics of deformable block structures, Eng. Comput. 9 (2) (1992) 157–168.

[39] B. Damjanac, P. Cundall, Application of distinct element methods to simulation of hydraulic fracturing in naturally fractured reservoirs, Comput. Geotech. 71 (JAN.) (2016) 283–294.

[40] Y. Ben, J. Xue, Q. Miao, Y. Wang, G.-H. Shi, Simulating hydraulic fracturing with discontinuous deformation analysis, in: 46th US Rock Mechanics / Geomechanics Symposium 2012, Vol. 1, 2012, pp. 683–690, cited By 11.

[41] S. Li, M. Zhao, Y. Wang, Y. Rao, A new numerical method for dem –block and particle model, Int. J. Rock Mech. Min. Sci. 41 (2004) 414–418, Proceedings of the ISRM SINOROCK 2004 Symposium.

[42] C. Feng, S. Li, X. Liu, Y. Zhang, A semi-spring and semi-edge combined contact model in CDEM and its application to analysis of jiweishan landslide, J. Rock Mech. Geotech. Eng. 6 (1) (2014) 26–35.

[43] R. Helmig, Node-centered finite volume discretizations for the numerical simulation of multiphase flow in heterogeneous porous media, Comput. Geosci. 4 (2000) 141–164, http://dx.doi.org/10.1023/A:1011559916309.

[44] S. Lee, A finite-volume method with hexahedral multiblock grids for modeling flow in porous media, Comput. Geosci. 6 (2002) 353–379, http://dx.doi.org/10.1023/A:1021287013566.

[45] A. Michel, A finite volume scheme for two-phase immiscible flow in porous media, SIAM J. Numer. Anal. 41 (4) (2003) 1301–1317.

[46] I. Lunati, P. Jenny, Multiscale finite-volume method for compressible multiphase flow in porous media, J. Comput. Phys. 216 (2) (2006) 616–636.

[47] V. Reichenberger, H. Jakobs, P. Bastian, R. Helmig, A mixed-dimensional finite volume method for two-phase flow in fractured porous media, Adv. Water Resour. 29 (7) (2006) 1020–1036.

[48] I. Lunati, Multiscale finite-volume method for density-driven flow in porous media, Comput. Geosci. 12 (2008) 337–350, http://dx.doi.org/10.1007/s10596-007-9071-9.

[49] C. Yan, H. Zheng, FDEM-Flow3D: A 3D hydro-mechanical coupled model considering the pore seepage of rock matrix for simulating three-dimensional hydraulic fracturing, Comput. Geotech. 81 (2017) 212–228.

[50] V.R. Voller, S. Peng, Y.F. Chen, Numerical Solution of Transient, Free Surface Problems in Porous Media, W.W. Norton, 1996.

[51] A.H.-D. Cheng, Poroelasticity, Springer International Publishing, 2016.

[52] E.V. Dontsov, F. Zhang, Calibration of tensile strength to model fracture toughness with distinct element method, Int. J. Solids Struct. (2018) S0020768318301860.

[53] A.D.O. Potyondy, B.P.A. Cundall, A bonded-particle model for rock, Int. J. Rock Mech. Min. Sci. 41 (8) (2004) 1329–1364.

[54] V.E. Dontsov, An approximate solution for a plane strain hydraulic fracture that accounts for fracture toughness, fluid viscosity, and leak-off, Int. J. Fract. 205 (2) (2017) 221–237.

[55] P. Tan, Y. Jin, K. Han, B. Hou, M. Chen, X. Guo, J. Gao, Analysis of hydraulic fracture initiation and vertical propagation behavior in laminated shale formation, Fuel 206 (oct.15) (2017) 482–493.